ORIGINAL PAPER



Geometric and electronic structure of a crystallographically characterized thiolate-ligated binuclear peroxo-bridged cobalt(III) complex

Maksym A. Dedushko¹ · Dirk Schweitzer¹ · Maike N. Blakely¹ · Rodney D. Swartz¹ · Werner Kaminsky¹ · Julie A. Kovacs¹

Received: 8 May 2019 / Accepted: 11 July 2019 / Published online: 24 July 2019 © Society for Biological Inorganic Chemistry (SBIC) 2019

Abstract

In order to shed light on metal-dependent mechanisms for O–O bond cleavage, and its microscopic reverse, we compare herein the electronic and geometric structures of O_2 -derived binuclear Co(III)– and Mn(III)–peroxo compounds. Binuclear metal peroxo complexes are proposed to form as intermediates during Mn-promoted photosynthetic H_2O oxidation, and a Co-containing artificial leaf inspired by nature's photosynthetic H_2O oxidation catalyst. Crystallographic characterization of an extremely activated peroxo is made possible by working with substitution-inert, low-spin Co(III). Density functional theory (DFT) calculations show that the frontier orbitals of the Co(III)–peroxo compound differ noticeably from the analogous Mn(III)–peroxo compound. The highest occupied molecular orbital (HOMO) associated with the Co(III)–peroxo is more localized on the peroxo in an antibonding $\pi^*(O-O)$ orbital, whereas the HOMO of the structurally analogous Mn(III)–peroxo is delocalized over both the metal d-orbitals and peroxo $\pi^*(O-O)$ orbital. With low-spin d0 Co(III), filled d1 filled to the doubly occupied antibonding $\pi^*(O-O)$ orbital onto the metal ion. This is not the case with high-spin d1 Mn(III), since these orbitals are half-filled. This weakens the peroxo O–O bond of the former relative to the latter.

Keywords Dioxygen activation · Transition-metal peroxo chemistry · Electronic structure · X-ray crystallography

Introduction

Photosynthesis is one of the most important biochemical processes for maintaining aerobic life on this planet [1, 2]. This process involves the capture of solar energy and storage in chemical bonds via the catalytic oxidation of H_2O , the extraction of electrons, and formation of O_2 as a byproduct [3–6]. Nature had three billion years to refine this highly efficient Mn-containing catalyst, which is referred to as the oxygen evolving complex (OEC). The OEC consists of a $CaMn_3O_4$ cubane with an additional dangling Mn ion. Insights into the mechanism of water oxidation and O_2

Electronic supplementary material The online version of this article (https://doi.org/10.1007/s00775-019-01686-x) contains supplementary material, which is available to authorized users.

evolution, as well as its microscopic reverse, would contribute to the development of solar fuel cells. The O-O bondforming step is not well understood [7] since it follows the rate-determining step [8-12]. An unobserved Mn-peroxo intermediate is proposed to form [9–11], followed by the rapid release of O₂ [13]. Despite the fundamental importance of Mn-dioxygen chemistry, it remains relatively unexplored [14-16]. Small molecules provide an advantage in that lower temperatures can be accessed by using organic solvents, thereby providing an opportunity to observe metastable intermediates. Mononuclear Mn-peroxo complexes include side-on η^2 -bound peroxo [Mn^{III}(O₂)(13-TMC)]⁺ [17], and $[Mn^{III}(O_2)\kappa^4 - N_4py]^+$ [18]. There are fewer examples of binuclear Mn-peroxo compounds, and no examples of Mn clusters containing a coordinated peroxo. Our group reported the first example of a spectroscopically and structurally characterized, metastable binuclear peroxo-bridged Mn(III) complex derived from dioxygen [14, 19]. In addition, we have examined the effect of coordination environment on peroxo O–O bond lengths [20].



[☑] Julie A. Kovacs kovacs@uw.edu

The Department of Chemistry, University of Washington, Box 351700, Seattle, WA 98195-1700, USA

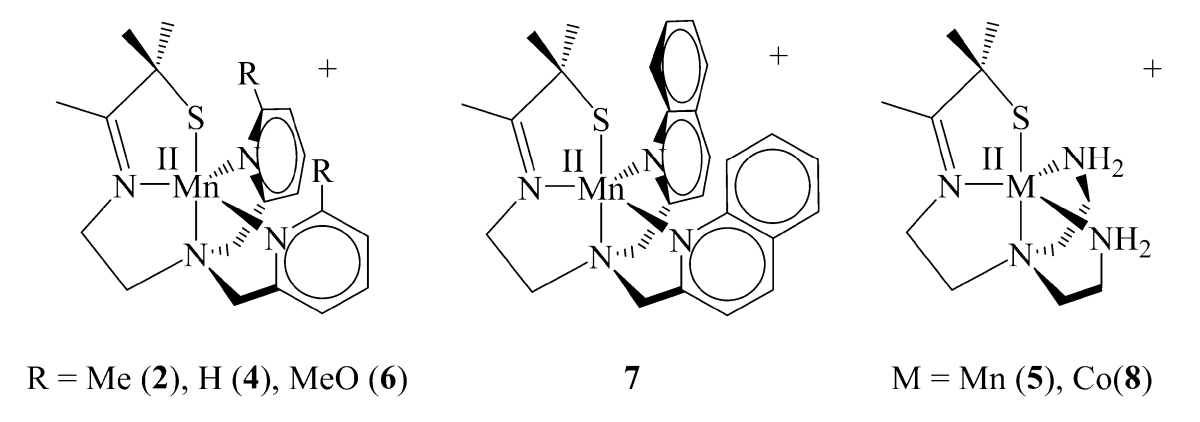
The inherent instability and reactive nature of dinuclear Mn(III)-peroxo complexes, both posited in nature and their synthetic analogues, renders the experimental investigation of their electronic and geometric structures difficult. Most of the reported Mn(III)-peroxo complexes are mononuclear with a peroxo moiety bound in a side-on (η^2) binding mode [15, 21–24]. There are very few examples of structurally characterized multi-nuclear Mn(III)–peroxo complexes [25]. We reported the first crystallographically characterized binuclear example, $\{[Mn^{III}(S^{Me2}(6-Me-DPEN))]_2(\mu-O_2)\}^{2+}(1)$ [19] derived from O₂. Reduced [Mn^{II}(S^{Me2}(6-Me-DPEN))]⁺ (2) binds dioxygen on the millisecond timescale to form a superoxo intermediate [19], which then converts to 1, en route to a binuclear μ -oxo end-product, {[Mn^{III}(S^{Me2}(6-Me-DPEN))]₂(μ -O)}²⁺ (**3**) [**14**, **19**]. The isolation of peroxo complex 1 was possible because the rate-determining step was determined to be the O-O bond-cleaving step [19]. The N-heterocycles (N^{Ar}) of [Mn^{II}(S^{Me2}(6-Me-DPEN))]⁺ (2) can be derivatized providing a convenient method for determining how steric and electronic properties affect the reactivity and relative stability of metastable dioxygen intermediates [19]. Manganese-dioxygen intermediates are not observed in the absence of steric bulk, for example with a H-substituent in the 6-position, [Mn^{II}(S^{Me2}(6-H-DPEN))]⁺ (4), or with primary amines in the ligand scaffold, [Mn^{II}(S^{Me2}N₄(tren))]⁺ (5). Our group has shown that steric bulk increases metal ion Lewis acidity by lengthening metal-ligand bonds, resulting in a stronger peroxo O-O bond [26].

More recent work by our group has led to the observation of two new metastable peroxo intermediates formed in the reaction between O_2 and thiolate-ligated Mn(II) derivatives (Fig. 1) of **2**, [Mn^{II}(S^{Me2}(6-MeO-DPEN))]⁺ (**6**) and [Mn^{II}(S^{Me2}(quinoEN))]⁺ (**7**) [20]. Changing the steric bulk and electron donor character of the ligand was shown to affect the barriers to O_2 binding and release, as well as O–O bond cleavage [20]. The less sterically encumbered 6-MeO-pyridine complex **6** binds O_2 more readily than the

other derivatives, **2** and **7**, and O_2 release from the superoxo is more favored. In addition, the 6-MeO-pyridine complex forms a total of four metastable intermediates with dioxygen, two of which follow a peroxo [20]. Thiolate ligands (RS⁻) were incorporated, because they have been shown to lower the activation barrier to O_2 binding [27, 28], as well as provide a convenient spectroscopic handle for observing reactive dioxygen intermediates [29].

The photosynthetic OEC's dioxygen-evolving properties can also be mimicked by cobalt complexes, the most notable example being Nocera's bioinspired artificial leaf [5, 30]. Discrete molecular Co_4O_4 cubane clusters, such as $[Co_4O_4(OAc)_4(py)_4]^+$, have also been shown to evolve O_2 upon the addition of OH^- [31]. A Co-peroxo is proposed to form as an intermediate, however, it was not observed. The mechanism is proposed to involve an oxidized trapped valence $Co^{III}_2Co^{IV}_2$ cubane cluster, and coupling between two oxyls on an adjacent Co^{IV}_2 pair $(O-Co^{IV}_2-Co^{IV}_2-O \rightarrow \bullet O-Co^{III}_2-Co^{III}_2-O \bullet)$ to afford an unobserved $Co^{III}_2-O-O-Co^{III}_2$ peroxo [30].

The mechanism for the O–O bond-forming step is likely to be different for Co and Mn, given that the oxo wall separates them [32]: the former is almost certain to proceed via an oxyl coupling mechanism [12], whereas the latter could proceed via a nucleophilic attack mechanism involving Mn(V)=O and M-OH (M=Ca(II) or Mn(III)) intermediates [33]. Developing a better understanding of the geometric and electronic structural differences between Mn(III) and Co(III) peroxo complexes, and the properties critical to O₂ release [12], is likely to shed more light on these reactions, and provide insight into metal-dependent mechanisms. There are many examples of synthetic Co(II) complexes that readily react with molecular O₂ at room temperature to form isolable dinuclear μ-peroxo Co(III) complexes, including a crystallographically characterized pac-man Schiff-base calixpyrroleligated binuclear Co(III) peroxo [34], and a crystallographically characterized fused pincer-ligated binuclear Co(III)





peroxo complex [35–40]. However, there are few (if any) structurally analogous pairs of binuclear μ -peroxo-bridged Co(III) and Mn(III) complexes. Whereas Mn(III) peroxo complexes are metastable, the added stability of low-spin d^6 transition-metal complexes is likely to stabilize a Co(III) peroxo, making it easier to obtain structural information. Described herein, is a crystallographically characterized, O₂-derived thiolate-ligated Co(III)- μ -peroxo complex, which is structurally analogous to our previously reported series of O₂-derived Mn–peroxo complexes [19].

Experimental

General methods

All manipulations were performed using Schlenk-line techniques or under a N₂ atmosphere in a glovebox. Reagents and solvents purchased from commercial vendors were of highest available purity and were used without further purification unless otherwise noted. MeOH (Mg(OMe)₂) was dried and distilled prior to use. Acetonitrile, Diethyl ether, and THF were rigorously degassed and purified using solvent purification columns housed in a custom stainlesssteel cabinet and dispensed by a stainless-steel Schlenk-line (GlassContour). $[Co^{II}(S^{Me2}N_4(tren))](PF_6)$ (8) was prepared according to literature procedures [41]. NMR spectra were recorded on a Bruker DPX 500 FTNMR spectrometer and referenced to the residual protio solvent. Electrosprayionization mass spectra were obtained on a Bruker Esquire Liquid Chromatograph-Ion Trap mass spectrometer. Cyclic voltammograms were recorded in MeCN solutions with Bu₄N(PF₆) (0.100 M) as the supporting electrolyte, using an EG&G Princeton Applied Research potentiostat with a glassy carbon working electrode, an SCE reference electrode, and a platinum auxiliary electrode. Electronic absorption spectra were recorded using a Hewlett-Packard 8453 diode array spectrometer. Elemental analyses were performed by Atlantic Microlab, Inc. (Norcross, GA).

Synthesis of $[Co^{III}(S^{Me2}N_4(tren))]_2(trans-\mu-1,2-O_2)$ (PF₆)₂·MeCN (9)

Reduced [Co^{II}(S^{Me2}N₄(tren))](PF₆) (**8**) (317 mg, 0.71 mmol) was dissolved in 100 mL of acetonitrile. The solution was exposed to air at room temperature and left to stir overnight. The dark red solution was evaporated to dryness, and the resulting red powder was washed with diethyl ether over a frit. The remaining solid was dissolved in 10 mL acetonitrile and layered with 30 mL of diethyl ether. The two layers were allowed to diffuse overnight at $-40\,^{\circ}\text{C}$ to afford red crystals of **9**. ESI–MS: calculated m/z for [C₂₂H₅₀Co₂N₈O₂S₂]²⁺ or [C₁₁H₂₅CoN₄OS]⁺ = 320.1 found m/z = 320.0. Electronic

absorption spectrum (MeCN): λ_{max} (nm) (ε (M⁻¹cm⁻¹)): 270(6500). ¹H NMR (500 MHz, CD₃CN) δ ppm 1.45 (s, 6H), 2.05 (s, 3H), 2.44 (s, 2H), 2.72 (dd, J=11.07, 4.37 Hz, 2H), 2.78 (q, J=6.38 Hz, 2H), 3.00 (s, 2H), 3.33 (dd, J=12.00, 5.44 Hz, 2H), 3.40 (t, J=8.50, 8.50 Hz, 2H), 3.66 (t, J=7.22, 7.22 Hz, 2H). Reduction potential (MeCN, vs. SCE): +220 mV (reversible). Elemental analysis for C₂₂H₅₀Co₂F₁₂N₈O₂P₂S₂ Calcd: C, 28.39; H, 5.42; N, 12.04. Found: C, 28.86; H, 5.41; N, 12.92.

X-ray crystallographic structure determination

A $0.19 \times 0.17 \times 0.14$ mm³ black prism of [Co(III) $(S^{Me2}N_4(tren))]_2(trans-\mu-1,2-O_2)(PF_6)_2\cdot MeCN$ (9) was mounted on a glass capillary with oil. Data were collected at -143 °C on a Nonius Kappa CCD single crystal X-ray diffractometer, Mo Kα-radiation. Crystal-to-detector distance was 30 mm and exposure time was 15 s per degree for all sets. The scan width was 2°. Data collection was 94.5% complete to 29.61° in θ and 96.9% complete to 25° in θ . A total of 18,295 partial and complete reflections were collected covering the indices, h = -9 to 8, k = -13 to 14, l = -15 to 14. 6556 reflections were symmetry independent and the $R_{int} = 0.0408$ indicated that the data were above average quality (0.07). Indexing and unit cell refinement indicated a triclinic P lattice. The space group was found to be P-1 (no. 2). The data for 9 were integrated and scaled using hkl-SCALEPACK [42, 43]. Solution by direct methods (SHELXS, SIR97) produced a complete heavy atom phasing model consistent with the proposed structure [44, 45]. The structure was completed by difference Fourier synthesis with SHELXL [46, 47]. Scattering factors are from Waasmair and Kirfel [11]. Hydrogen atoms were placed in geometrically idealized positions and constrained to ride on their parent atoms with C—H distances in the range 0.95–1.00 Angstrom. Isotropic thermal parameters Ueq were fixed such that they were 1.2 Ueq of their parent atom Ueq for CHs and 1.5 Ueq of their parent atom Ueq in case of methyl groups. All non-hydrogen atoms were refined anisotropically by fullmatrix least-squares. Final solution plotted using ORTEP and POV-Ray programs [48, 49].

Computational details

Calculations were performed using the ORCA v.4.0.0 quantum chemistry package developed by Neese and coworkers [50]. Geometry optimizations employed the B3LYP hybrid functional and 6-311G basis set for all complexes. Tight convergence criteria were required for self-consistent field (SCF) solutions. The Grid4 (GridX4) integration grid size, and the conductor-like polarizable continuum model (CPCM) were used for geometry optimizations [51].



Crystallographic coordinates were used as a starting point for geometry optimizations of peroxo $\{[Co^{III}(S^{Me2}N_4(tren))]_2(trans-\mu-1,2-O_2)\}^{2+}$ (9) using the B3LYP/6-311G functional/basis set. Details regarding the theoretical calculations for peroxo-bridged $[Mn^{III}(S^{Me2}N_4(quinoEN)]_2(\mu-O_2)(BPh_4)_2$ (10) and $\{[Mn^{III}(S^{Me2}N_4(6-MeO-DPEN)]_2(\mu-O_2)\}^{2+}$ (11) are reported elsewhere [20]. Canonical molecular orbital isosurfaces were visualized at an isovalue of 0.03 a_0^3 using UCSF Chimera software [52].

Results and discussion

The reaction between [Co^{II}(S^{Me2}N₄(tren))](PF₆) (8) and dioxygen (O₂) in MeCN at ambient temperature results in a color change from pale yellow to red, with the concomitant growth of peaks at $\lambda_{\text{max}}(\varepsilon \, (\text{M}^{-1} \, \text{cm}^{-1})) = 280 \, (11,350), 385$ (3085), and 485 (1250) nm (Figure S2). The ¹H NMR of this dioxygen product, 9 (Figure S3), only contains peaks in the diamagnetic region of the spectrum, consistent with oxidation of the S = 3/2 Co(II) precursor [41] to low-spin (L.S.) S=0 Co(III). The ESI-MS of 9 (Fig. 2) displays a peak at m/z = 320.0, consistent with either the addition of two oxygen atoms to a dicationic dimer (M+32), where M=608.2, z=2), or the addition a single oxygen atom to a monocationic monomer (M+16), where M=304.1, z=1). These two possibilities would be distinguishable based on their isotope distribution pattern. As shown in the simulated spectrum of Figure S1, peaks would be separated by 1/2 mass unit for a dicationic dimer, versus one mass unit for a monocationic monomer. The experimental data would therefore be

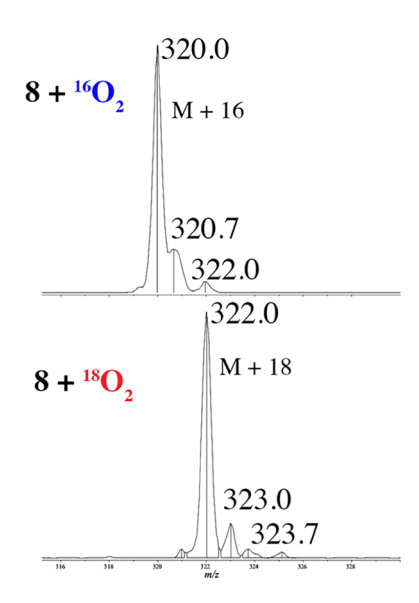


Fig. 2 ESI-MS of peroxo-bridged 9 derived from $^{16}\mathrm{O}_2$ (top) and $^{18}\mathrm{O}_2$ (bottom)



consistent with the former. This was consistently the case across a wide range of applied skim voltages (4–10 V to 30–70 V), implying that we are looking at either a Co–peroxo with a remarkably weak O–O bond, or a Co–oxo. The reaction of **8** with isotopically labeled 18 O₂ results in a peak shift to $m/z = 322.0 \ (M+18)$, consistent with incorporation of one oxygen atom, derived from dioxygen.

Crystallization from MeCN/Et₂O afforded single crystals of 9 suitable for X-ray crystallography. As shown in the ORTEP diagram of Fig. 3, {[Co^{III}(S^{Me2}N₄(tren))]₂ (trans- μ -(9) is binuclear and contains an O_2 moiety bridging between two Co ions in a trans- μ -1,2-configuration. The Co–S bond length of **9** (2.2180 (9) Å) is 0.083 Å shorter than the reduced precursor 8 (Co–S = 2.3006(7) Å), and the average Co-N bond length distance is 0.173 Å shorter than the corresponding distance in 8. More importantly, the Co-S, average Co-N, and Co-O bond lengths in 9 are comparable (Table 1) to the previously characterized hydroxo complex $[Co^{III}(S^{Me2}N_4(tren))(OH)]^+$ (12) [53], consistent with the oxidation of the high-spin Co(II) (S = 3/2) ion in 8 to a low-spin Co(III) (S=0) ion in **9**. The Co-O bond length in 9 (1.899 (2) Å) is comparable to that of 12, as well as other previously reported Co(III) peroxo compounds [35, 54, 55]. The O–O bond length of dicationic 9 (1.482(4) Å) is consistent with a peroxo, but is 0.054 Å longer than that of neutral (B₂pz₄Py)Co^{III}-O-O-Co^{III}(B₂pz₄Py), which contains two dianionic ligands [50]. This indicates that the peroxo in 9 is highly activated. The two halves of the dimer are twisted relative to each other with a dihedral angle of 180°, and the plane containing the Co(III)-O-O-Co(III) core is approximately perpendicular to the plane containing two Co-S bonds. The Co-O-O bond angle (114°) is more obtuse than the corresponding Mn–O–O angle of 1 (Table 1), but is comparable to most Co^{III}-peroxo compounds [35, 54-61].

Structure **9** is analogous to our previously reported crystallographically characterized $trans-\mu-1,2$ -peroxo bridged Mn(III) complex, {[Mn^{III}(S^{Me2}N₄(6-Me-DPEN)]₂($trans-\mu-1,2-O_2$)}²⁺ (**1**) [19], as well as two additional

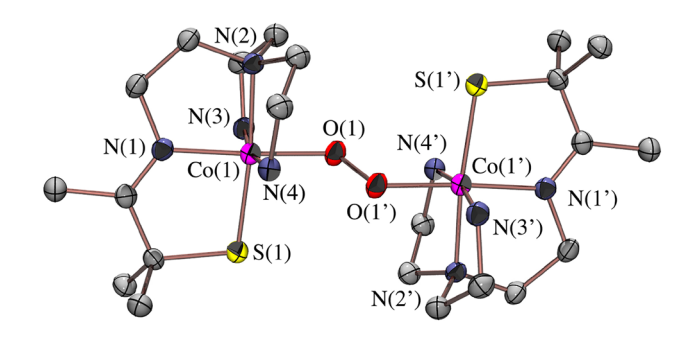


Fig. 3 ORTEP of peroxo-bridged $\{[Co^{III}(S^{Me2}N_4(tren))]_2(trans-\mu-1,2-O_2)\}^{2+}$ (9) showing 50% probability ellipsoids and the atom labeling scheme. Hydrogens are omitted for clarity

Table 1 Selected bond distances (Å) and bond angles (deg) for $[Co^{II}(S^{Me2}N_4(tren))](PF_6)$ (**8**), peroxo-bridged $[Co^{III}(S^{Me2}N_4(tren))]_2(trans-<math>\mu$ -1,2-O₂)(PF₆)₂·MeCN (**9**), peroxo-bridged $[Mn^{III}(S^{Me2}N_4(tren))]_2(trans-<math>\mu$ -1)₂·MeCN (**9**), peroxo-bridged $[Mn^{III}($

 $\begin{array}{l} (6\text{-Me-DPEN}))]_{2}(trans-\mu-1,2\text{-O}_{2})(BPh_{4})_{2}\cdot 2CH_{3}CH_{2}CN \\ \text{hydroxo bound } [Co^{III}(S^{Me2}N_{4}(tren))(OH)](PF_{6}) \ \textbf{(12)}^{54} \end{array}$

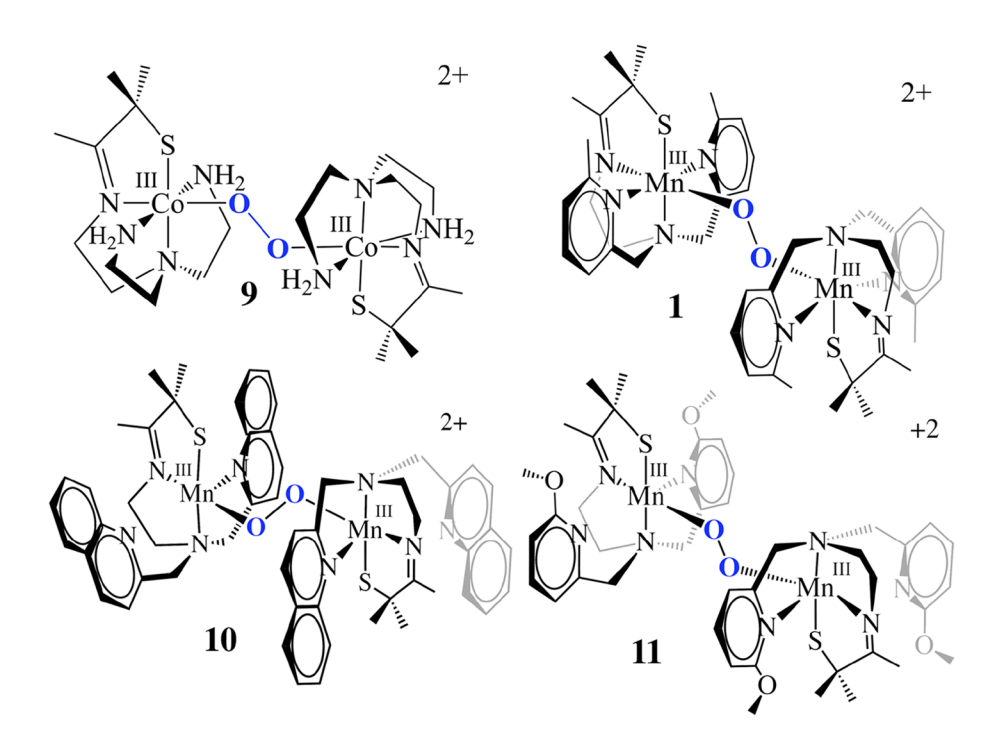
(1), and

	8 (d^7 , $S = 3/2$; H.S.)	$9 (d^6, S = 0; L.S.)$	$1 (d^4, S = 2; H.S.)$	12
M(1)–S(1)	2.3006 (7)	2.2180 (9)	2.275 (11)	2.217 (3)
M(1)–N(1)	2.050 (2)	1.900 (2)	2.040 (3)	1.892 (8)
M(1)-N(2)	2.223 (2)	1.978 (3)	2.203 (3)	1.971 (8)
M(1)–N(3)	2.107 (2)	1.935 (2)	2.410(3)	1.935 (6)
M(1)–N(4)	2.086 (2)	1.963 (2)	2.492 (3)	1.935 (6) ^a
M(1)–O(1)	N/A	1.899 (2)	1.832 (3)	1.869 (6)
O(1)–O(1')	N/A	1.482 (4)	1.452 (5)	N/A
M(1)···O(1')	N/A	2.845	2.481	N/A
$M(1)\cdots M(1')$	N/A	4.604	4.113	N/A
M(1)–O(1)–O(1')	N/A	114.0 (2)	97.5 (6)	N/A
O(1)-M(1)-S(1)	N/A	94.88 (7)	85.12 (9)	95.8 (2)
O(1)-M(1)-N(3)	N/A	90.9 (1)	92.4 (1)	87.7 (2)
O(1)-M(1)-N(1)	N/A	174.24 (9)	165.5 (1)	178.0 (3)
O(1)-M(1)-N(2)	N/A	90.61 (9)	111.1 (1)	90.0(3)
S(1)-M-N(2)	163.96 (6)	174.24 (7)	163.3 (1)	174.3 (2)
S(1)-M-N(3)	112.25 (6)	94.10 (8)	109.0 (1)	94.23 (17)
S(1)-M-N(4)	106.90 (6)	94.05 (8)	105.6 (1)	94.23 (17) ^a
N(1)-M-N(4)	125.14 (8)	92.0 (1)	101.7 (1)	92.17 (17) ^a

 $^{^{}a}N(4) = N(3')$ for this structure, since a crystallographic mirror plane relates the two atoms (N(3) and N(3')

spectroscopically characterized Mn(III)–peroxo compounds, [Mn^{III}(S^{Me2}N₄(quinoEN)]₂(μ –O₂)(BPh₄)₂ (**10**) and {[Mn^{III}(S^{Me2}N₄(6-MeO-DPEN))]₂(μ –O₂)}²⁺ (**11**), for which

spectroscopically calibrated DFT-calculated structures are available (Scheme 1) [20]. Relative to **1** (1.452 (5)), the peroxo O–O bond of bimetallic Co(III)–peroxo **9** is 0.03 Å



 $\begin{array}{l} \textbf{Scheme 1} \quad \text{ChemDraw sketches of } \{[Co^{III}(S^{Me2}N_4(tren))]_2(\textit{trans-μ-$1,2-$O}_2)\}^{2+} \quad \textbf{(9)}, \ \{[Mn^{III}(S^{Me2}N_4(6-Me-DPEN)]_2(\textit{trans-μ-$1,2-$O}_2)\}^{2+} \quad \textbf{(1)},^{26} \\ \{[Mn^{III}(S^{Me2}N_4(quinoEN))]_2(\mu-O_2)\}^{2+} \quad \textbf{(10)},^{19} \ \text{and} \ \{[Mn^{III}(S^{Me2}N_4(6-MeO-DPEN))]_2(\mu-O_2)\}^{2+} \quad \textbf{(11)},^{19} \\ \end{bmatrix} \end{array}$



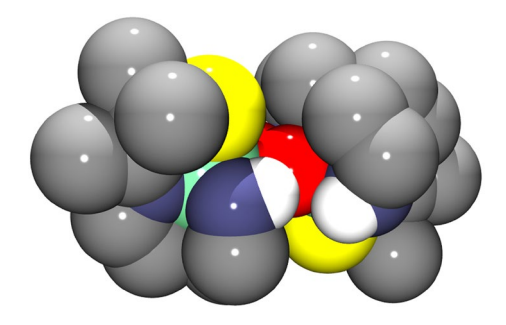
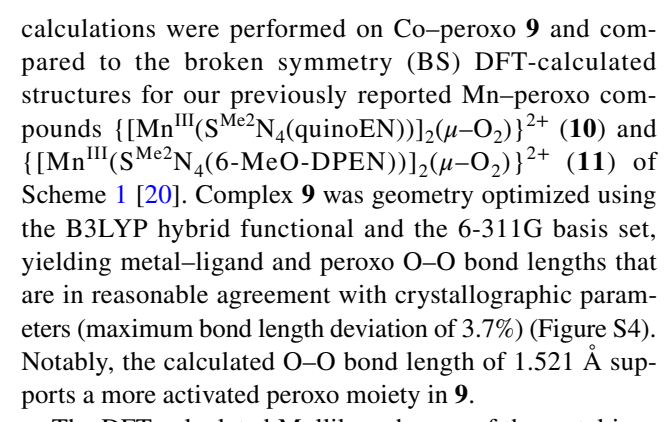


Fig. 4 Space-filling diagram of peroxo-bridged $\{[Co^{III}(S^{Me2}N_4(tren))]_2(trans-\mu-1,2-O_2)\}^{2+}$ (9) showing N–H hydrogen bonding to the peroxo (red)

longer, and closer to that of O_2^{2-} (1.49 Å) [62], indicating that the peroxo is more activated in 9. An activated O-O bond should be susceptible to cleavage, consistent with our inability to observe the intact dimer by mass spectrometry (vide supra). Only half of the dimer, consisting of a monocationic cobalt-oxo, is detected by ESI-MS, even at the lowest applied skim voltage (4–10 V) (Fig. 2). Peroxos are π -donors that can be stabilized via the removal of antibonding electron density from the peroxo π^* orbitals, via π -back-donation into a metal ion t_{2a} d-orbital. With low-spin d^6 Co(III), the π -symmetry $t_{2\sigma}$ orbitals are filled, whereas they are only halffilled with a high-spin d^4 Mn(III) ion. If the t_{2g} orbitals are filled, then the above described pathway for O-O bond stabilization is not available. In addition, with cobalt peroxo 9 there are two short H-bonds $(N(2)-H(2E)\cdots O(1))=2.051$ A) to the bridging peroxo oxygens (Fig. 4), which are absent in the Mn(III) compound. It is possible that these H-bonds also contribute to O-O bond activation in 9. However, there are other examples of bridging Co peroxo compounds lacking H-bonds with similar distances [35, 63].

We recently showed that metal ion Lewis acidity can influence peroxo O–O bond lengths by facilitating π -backdonation of electron density from the peroxo π^* orbital [16, 26]. Metal ion Lewis acidity was found to depend on the steric properties of the ligand scaffold. Ligands with sterically demanding substituents on the aryl ring (e.g., 2, 6, and 7, Fig. 1) were found to possess unusually long M... N^{Ar} distances in the corresponding M(III) derivatives [64]. Elongation of the Mn···N^{Ar} distances was shown to increase metal ion Lewis acidity and create a virtual coordinatively unsaturated metal ion [16, 26]. This facilitates π -backdonation from the filled peroxo $\pi^*(O-O)$ orbital to the metal ion, resulting in a shorter peroxo O-O bond [16]. With less sterically demanding primary amines (e.g., 5 and 8, Fig. 1), on the other hand, M-N (M = Mn or Co) distances in the corresponding M(III) derivatives were found to be significantly shorter.

To gain more insight into the electronic structure differences governing peroxo O-O bond activation, DFT



The DFT-calculated Mulliken charges of the metal ions in 9 (+1.45), 11 (+1.59), and 10 (+1.60) indicate that metal ion Lewis acidity does not necessarily follow the expected periodic trends of Co>Mn. Steric constraints imposed by the ligand elongate two of the Mn···N^{Ar} distances [20] for the Mn–peroxo complexes $\{[Mn^{III}(S^{Me2}N_4(quinoEN))]_2$ $(\mu - O_2)$ ²⁺ (**10**, Scheme 1) and {[Mn^{III}(S^{Me2}N₄(6-MeO-DPEN))]₂- $(\mu$ -O₂) $\}^{2+}$ (11, Scheme 1), and this is reproduced by the calculations. Conversely, the calculated electron density localized on the bridging peroxo oxygens is higher with Co-containing 9 (-0.56), relative to Mn-containing 11 (-0.48) and 10 (-0.49). This trend reflects the fact that the $\pi^*(O-O)$ orbital cannot π -back-donate into the filled t_{2g} orbitals of a L.S. d^6 Co(III) ion, resulting in a the localization of electron density on the peroxo oxygens and destabilization of the peroxo O-O bond. An analysis of the frontier orbital of both the Co and Mn-peroxo complexes, 9 and 11 (Fig. 5), corroborates the strong dependence of the extent of O-O bond activation on the electronic properties of the metal ion. The highest occupied molecular orbital (HOMO) contains significant $\pi^*(O-O)$ character for both Co-peroxo 9 and Mn-peroxo 11. However, the HOMO of Mn-peroxo $\{[Mn^{III}(S^{Me2}N_4(6-MeO-DPEN))]_2-(\mu-O_2)\}^{2+}$

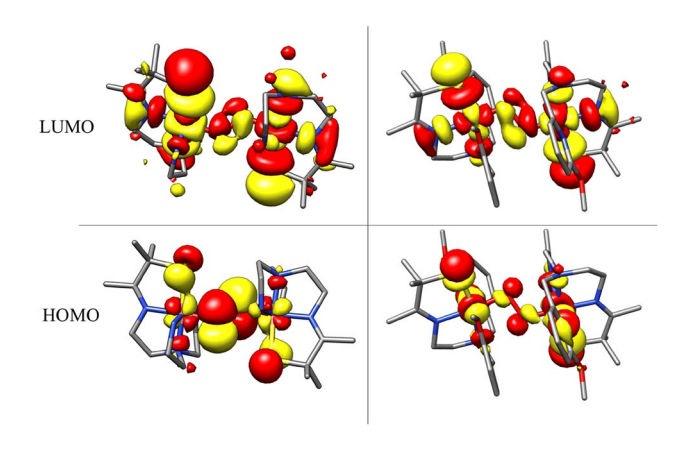


Fig. 5 Frontier orbitals of $Co^{III}(S^{Me2}N_4(tren))]_2(trans-\mu-1,2-O_2)\}^{2+}(9)$ (left) and $\{[Mn^{III}(S^{Me2}N_4(6-MeO-DPEN)]_2(trans-\mu-1,2-O_2)\}^{2+}(11)$ (right)¹⁹ visualized at an isovalue of 0.03 a_0^3



(11, Scheme 1) is fairly delocalized, extending over both the O–O π^* and singly occupied t_{2g} Mn d-orbitals (Fig. 5, right). This would be consistent with higher calculated Lewis acidity of the Mn ions in 11 as well as the observed stabilization of the peroxo O–O bond. The HOMO of Co–peroxo 9 (Fig. 5, left), however, is dominated by the $\pi^*(O-O)$ orbital and predominantly peroxo in character, consistent with lack of π -back-donation into the fully occupied Co t_{2g} d-orbitals (Fig. 5). The LUMO of both 9 and 11 is antibonding with respect to the M–O(peroxo) bond.

Conclusions

This work describes the structure and properties of a O₂-derived thiolate-ligated, peroxo-bridged Co(III) dimer and provides a comparison with structurally analogous peroxo-bridged Mn(III) dimers. It also provides a rationale for the effects that both electronic structural differences and the ligand scaffold can have on peroxo O-O bond activation. The electronic structure of the metal ion, as well as the metal ion Lewis acidity, is shown to have a profound impact on peroxo O-O bond activation and stability. The lack of steric bulk in the Co-peroxo compound is shown to decrease metal ion Lewis acidity relative to the Mn-peroxo compounds, resulting in a more activated peroxo O-O bond. In addition, with its completely filled π -symmetry $t_{2\sigma}$ set of orbitals, the L.S. d^6 Co(III) ion is incapable of providing stability to the peroxo O–O bond through π -back-donation from the $\pi^*(O-O)$. DFT calculations support this by showing that, with Co(III), the HOMO contains more electron density localized in the peroxo $\pi^*(O-O)$ orbital, relative to the HOMO of the structurally analogous Mn(III) peroxo complex, resulting in a more activated peroxo O–O bond. The substitution-inert character of the Co(III) ion facilitates the isolation of a significantly more activated peroxo. Insight into some of the key factors governing O-O bond activation can serve as a benchmark for future small-molecule design.

Acknowledgements We wish to thank the National Science Foundation (Division of Chemistry) for funding (CHE-1664682).

References

- 1. Leslie M (2009) Science 323(5919):1286
- 2. Barber J (2009) Chem Soc Rev 38(1):185
- Askerka M, Brudvig GW, Batista VS (2017) Acc Chem Res 50(1):41
- 4. Yano J, Yachandra V (2014) Chem Rev 114(8):4175
- 5. Nocera DG (2012) Acc Chem Res 45(5):767
- Cox N, Pantazis DA, Neese F, Lubitz W (2013) Acc Chem Res 46(7):1588
- 7. Renger GJ (2011) Photochem Photobiol B Biol 104(1-2):35

- Retegan M, Krewald V, Mamedov F, Neese F, Lubitz W, Cox N, Pantazis DA (2015) Chem Sci 7(1):72
- Cox N, Retegan M, Neese F, Pantazis DA, Boussac A, Lubitz W (2014) Science 345(6198):804
- Brudvig GW (2008) Philos Trans R Soc B Biol Sci 363(1494):1211
- Dismukes GC, Brimblecombe R, Felton GAN, Pryadun RS, Sheats JE, Spiccia L, Swiegers GF (2009) Acc Chem Res 42(12):1935
- 12. Betley TA, Wu Q, Van Voorhis T, Nocera DG (2008) Inorg Chem 47(6):1849
- Armstrong FA (2008) Philos Trans R Soc B Biol Sci 363(1494):1263
- Coggins MK, Brines LM, Kovacs JA (2013) Inorg Chem 52(21):12383
- Shook RL, Gunderson WA, Greaves J, Ziller JW, Hendrich MP, Borovik AS (2008) J Am Chem Soc 130(28):8888
- Rees JA, Martin-Diaconescu V, Kovacs JA, DeBeer S (2015) Inorg Chem 54(13):6410
- 17. Annaraj J, Cho J, Lee YM, Kim SY, Latifi R, De Visser SP, Nam W (2009) Angew Chem Int Ed 48(23):4150
- Geiger RA, Leto DF, Chattopadhyay S, Dorlet P, Anxolabéhère-Mallart E, Jackson TA (2011) Inorg Chem 50(20):10190
- Coggins MK, Sun X, Kwak Y, Solomon EI, Rybak-Akimova E, Kovacs JA (2013) J Am Chem Soc 135(15):5631
- Poon PCY, Dedushko MA, Sun X, Yang G, Toledo S, Hayes EC, Johansen A, Rees JA, Stoll S, Rybak-Akimova E, Kovacs JA (2019) J Am Chem Soc (accepted).
- 21. Seo MS, Kim JY, Annaraj J, Kim Y, Lee YM, Kim SJ, Kim J, Nam W (2007) Angew Chem Int Ed 46(3):377
- Vanatta RB, Strouse CE, Hanson LK, Valentine JS (1987) J Am Chem Soc 109(5):1425
- Kitajima N, Komatsiizaki H, Hikichi S, Osawa M, Moro-oka Y (1994) J Am Chem Soc 116(25):11596
- Singh UP, Sharma AK, Hikichi S, Komatsuzaki H, Moro-oka Y, Akita M (2006) Inorg Chim Acta 359(13):4407
- Bossek U, Weyhermiiller T, Wieghardt K, Nuber B, Weiss J (1990) J Am Chem Soc 112(17):6387
- Coggins MK, Martin-Diaconescu V, Debeer S, Kovacs JA (2013) J Am Chem Soc 135(11):4260
- 27. Brown CD, Neidig ML, Neibergall MB, Lipscomb JD, Solomon EI (2007) J Am Chem Soc 129(23):7427
- 28. Kovacs JA, Brines LM (2007) Acc Chem Res 40(7):501
- 29. Kovacs JA (2015) Acc Chem Res 48(10):2744
- Brodsky CN, Hadt RG, Hayes D, Reinhart BJ, Li N, Chen LX, Nocera DG (2017) Proc Natl Acad Sci 114(15):3855
- Smith PF, Hunt L, Laursen AB, Sagar V, Kaushik S, Calvinho KUD, Marotta G, Mosconi E, De Angelis F, Dismukes GC (2015) J Am Chem Soc 137(49):15460
- 32. Ballhausen CJ, Gray HB (1962) Inorg Chem 1:111
- Gao Y, Åkermark T, Liu J, Sun L, Åkermark B (2009) J Am Chem Soc 131(25):8726
- Volpe M, Hartnett H, Leeland JW, Wills K, Ogunshun M, Duncombe BJ, Wilson C, Blake AJ, McMaster J, Love JB (2009) Inorg Chem 48(12):5195
- 35. Schaefer WP, Marsh RE (1966) J Am Chem Soc 88(1):178
- 36. Sykes AG, Weil JA (1970) Prog Inorg Chem 13:1-106
- 37. Kotani H, Hong D, Satonaka K, Ishizuka T, Kojima T (2019) Inorg Chem 58(6):3676
- 38. Seo JS, Hynes RC, Williams D, Chin J (1998) J Am Chem Soc 120(38):9943
- Givaja G, Volpe M, Edwards MA, Blake AJ, Wilson C, Schröder M, Love JB (2007) Angew Chem Int Ed 46(4):584
- 40. Wang D, Lindeman SV, Fiedler AT (2015) Inorg Chem 54(17):8744



- Brines LM, Shearer J, Fender JK, Schweitzer D, Shoner SC, Barnhart D, Kaminsky W, Lovell S, Kovacs JA (2007) Inorg Chem 46(22):9267
- Otwinowski Z, Minor W (1997) In: Sweet RM, Carter CW (eds) Macromolecular crystallography, 1st edn. Academic Press, New York
- 43. Mackay S, Edwards C, Henderson A, Gilmore C, Stewart N, Shankland K, Donald A (1997) maXus 1.1, A computer program for the solution and refinement of crystal structures from X-ray diffraction data, University of Glasgow, Scotland, Nonius, The Netherlands, and MacScience, Japan (1997).
- Altomare A, Cascarano G, Giacovazzo C, Guagliardi A, Burla MC, Polidori G, Camalli M (1994) J Appl Crystallogr 27(3):435
- Altomare A, Burla MC, Camalli M, Cascarano GL, Giacovazzo C, Guagliardi A, Moliterni AGG, Polidori G, Spagna R (1999) J Appl Crystallogr 32(1):115
- Sheldrick GM (1997) SHELXS97 and SHELXL97. University of Göttingen, Göttingen, Program for Crystal Structure Solution and Refinement
- 47. Sheldrick GM (2015) Acta Crystallogr Sect C Struct Chem 71(Md):3
- Burnett MN, Johnson CK (1996) Oak Ridge National Laboratory Report ORNL-6895
- Persistence of Vision Pty. Ltd. (2013) Persistence of Vision Raytracer Version 3.7. Williamstown, Victoria, Australia
- 50. Neese F (2012) WIREs Comput Mol Sci 2:73
- 51. Barone V, Cossi M (1998) J Phys Chem A 102(11):1995
- Pettersen EF, Goddard TD, Huang CC, Couch GS, Greenblatt DM, Meng EC, Ferrin TE (2004) UCSF Chimera—A Visualization System for Exploratory Research and Analysis. J Comput Chem 25:1605–1612

- Swartz RD, Coggins MK, Kaminsky W, Kovacs JA (2011) J Am Chem Soc 133(11):3954
- Nurdin L, Spasyuk DM, Fairburn L, Piers WE, Maron L (2018) J Am Chem Soc 140(47):16094
- Ramprasad D, Gilicinski AG, Markley TJ, Pez GP (1994) Inorg Chem 33(13):2841
- Rigsby ML, Mandal S, Nam W, Spencer LC, Llobet A, Stahl SS (2012) Chem Sci 3(10):3058
- Ludovici C, Fröhlich R, Vogtt K, Mamat B, Lübben M (2003) Eur J Biochem 269(10):2630
- Howard-Jones AR, Adam V, Cowley A, Baldwin JE, Bourgeois D (2009) Photochem Photobiol Sci 8(8):1150
- Fukuzumi S, Mandal S, Mase K, Ohkubo K, Park H, Benet-Buchholz J, Nam W, Llobet A (2012) J Am Chem Soc 134(24):9906
- 60. Cho YI, Joseph DM, Rose M (2013) J Inorg Chem 52(23):13298
- Wang HY, Mijangos E, Ott S, Thapper A (2014) Angew Chem Int Ed 53(52):14499
- 62. Vaska L (1976) Acc Chem Res 9(5):175
- 63. Fritch JR, Christoph GG, Schaefer WP (1973) Inorg Chem 12(9):2170
- Coggins MK, Toledo S, Shaffer E, Kaminsky W, Shearer J, Kovacs JA (2012) Inorg Chem 51(12):6633

Publisher's Note Springer Nature remains neutral with regard to jurisdictional claims in published maps and institutional affiliations.

